DOI:
10.1088/1361-6560/aae758

Document Version
Peer reviewed version

Pixel-wise quantification of myocardial perfusion using spatial Tikhonov regularization

Judith Lehnert[1], Gerd Wübbeler[1], Christoph Kolbitsch[1,2], Amedeo Chiribiri[2], Loïc Coquelin[3], Géraldine Ebrard[3], Nadia Smith[4], Tobias Schaeffter[1,2], Clemens Elster[1]

[1]Physikalisch-Technische Bundesanstalt (PTB), Braunschweig and Berlin, Germany
[2]School of Biomedical Engineering and Imaging Sciences, Kings College London, UK
[3]Laboratoire National de Métrologie et d'Essai (LNE), Trappes, France
[4]National Physical Laboratory (NPL), Teddington, UK

E-mail: judith.lehnert@ptb.de

September 2018

Abstract. Quantification of myocardial perfusion by contrast-enhanced cardiovascular magnetic resonance imaging (CMR) aims for an observer independent and reproducible risk assessment of cardiovascular disease. Currently, the data used for the pixel-wise analysis of cardiac perfusion are either filtered prior to a fitting procedure, which inherently reduces the spatial resolution of data; or all pixels are considered without any regularization or prior filtering, which yields an unstable fit in the presence of low signal-to-noise ratio. Here, we propose a new pixel-wise analysis based on spatial Tikhonov regularization which exploits the spatial smoothness of the data and ensures accurate quantification even for images with low signal-to-noise ratio. The regularization parameter is determined automatically by an L-curve criterion. We study the performance of our method on a numerical phantom and demonstrate that the method reduces significantly the root-mean square error in the perfusion estimate compared to a non-regularized fit. In patient data our method allows us to recover the myocardial perfusion and to distinguish between healthy and ischemic regions.

Keywords: Cardiovascular magnetic resonance, Dynamic contrast-enhanced magnetic resonance imaging, Myocardial perfusion, Perfusion quantification, Spatial resolution, Fermi method, Tikhonov regularization, Singular value decomposition

Submitted to: *Phys. Med. Biol.*

1. Introduction

Myocardial perfusion imaging is a non-invasive technique used in the diagnosis, management, and prognosis of cardiovascular disease as regions of underperfused myocardium are a reliable indicator of the presence of significant coronary artery disease.

In myocardial perfusion imaging by first-pass contrast-enhanced cardiovascular magnetic resonance (CMR) signal intensity variations in the MR image after the injection of a contrast agent are monitored over time. First-pass contrast-enhanced CMR in the myocardium is a well-established non-invasive technique to identify ischemic regions by visual assessment (Jerosch-Herold 2010). Quantitative estimation of myocardial perfusion is the focus of vivid research (Jerosch-Herold, Seethamraju, Swingen, Wilke & Stillman 2004, Jerosch-Herold 2010, Attili, Schuster, Nagel, Reiber & van der Geest 2010, Gupta, Kirişli, Hendriks, van der Geest, van de Giessen, Niessen, Reiber & Lelieveldt 2012, Sourbron & Buckley 2012, Kellman, Hansen, Nielles-Vallespin, Nickander, Themudo, Ugander & Xue 2017, Hsu, Jacobs, Benovoy, Ta, Conn, Winkler, Greve, Chen, Shanbhag, Bandettini et al. 2018) as it would allow for observer independent and reproducible evaluation of the hemodynamic status and, thus, for more objective risk prediction in the assessment of cardiovascular disease. However, quantification of myocardial perfusion is still faced with multiple challenges and is, therefore, currently not part of clinical routine. Owing to the low signal-to-noise ratio (SNR) of the images most studies on perfusion quantification focus on segment-wise quantification (see Fig. 1(a)) entailing the risk of missing small perfusion defects. This is in particular unfortunate as averaging over segments means losing the high spatial resolution ($1.4-3$ mm in-plane (Plein, Schwitter, Suerder, Greenwood, Boesiger & Kozerke 2008, Schwitter, Wacker, van Rossum, Lombardi, Al-Saadi, Ahlstrom, Dill, Larsson, Flamm, Marquardt et al. 2008, Greenwood, Maredia, Younger, Brown, Nixon, Everett, Bijsterveld, Ridgway, Radjenovic, Dickinson et al. 2012, Chiribiri, Schuster, Ishida, Hautvast, Zarinabad, Morton, Otton, Plein, Breeuwer, Batchelor et al. 2012, Dabir, Child, Kalra, Rogers, Gebker, Jabbour, Plein, Yu, Otton, Kidambi et al. 2014)) of CMR, which is one of the main advantages of this technique. High spatial resolution allows for the detection of sub-endocardial layer ischaemia, which is difficult to identify in single-photon emission computed tomography (SPECT) and positron emission tomography (PET) images due to the relative limited spatial resolution of these techniques (Lee, Simonetti, Harris, Holly, Judd, Wu & Klocke 2004, Gupta et al. 2012).

Pixel-wise quantification has been proposed more recently for the quantification of myocardial perfusion (Zarinabad, Chiribiri, Hautvast, Ishida, Schuster, Cvetkovic, Batchelor & Nagel 2012, Hsu, Groves, Aletras, Kellman & Arai 2012, Miller, Naish, Ainslie, Tonge, Tout, Arumugam, Banerji, Egdell, Clark, Weale, Steadman, McCann, Ray, Parker & Schmitt 2014, Sammut, Zarinabad, Wesolowski, Morton, Chen, Sohal, Carr-White, Razavi & Chiribiri 2015, Villa, Sammut, Shome, Razavi, Plein & Chiribiri 2016, Kellman et al. 2017, Hsu et al. 2018) (see Fig. 1(b)). Since fitting the signal from a single pixel is challenging due to the low SNR, a priori filtering in the spatial domain (Kellman et al. 2017) or in the spatial and temporal domain (Zarinabad et al. 2012) has been proposed. However, there are several drawbacks of filtering the data a priori. Inherently, this decreases the spatial resolution of the results. Since filtering and fitting are separate steps, they cannot be balanced against each other, and errors introduced during the filtering cannot be reversed. Furthermore, the filter parameters

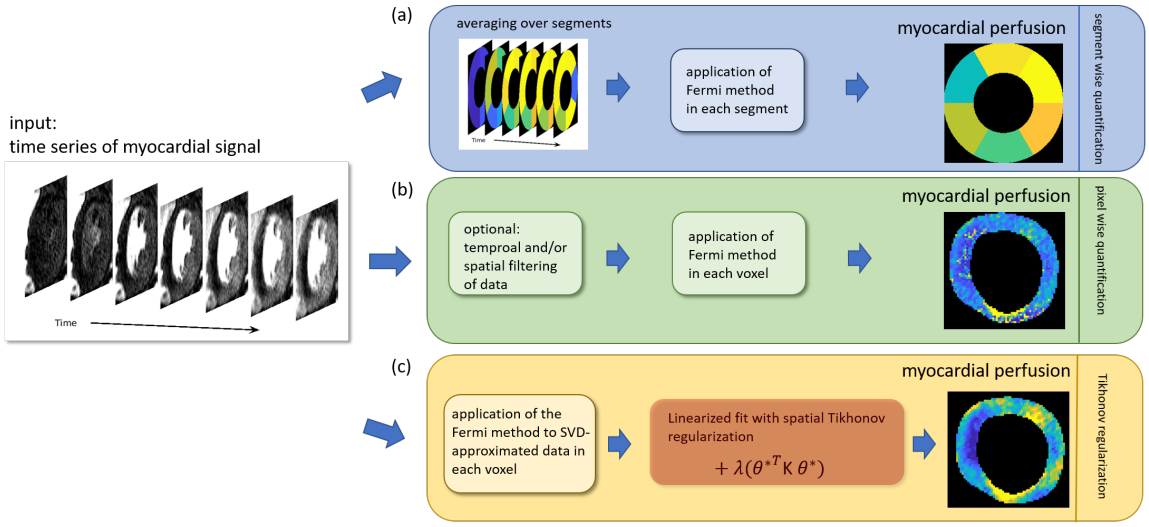

Figure 1. Schematic image of different methods in the quantification of myocardial perfusion. (a) Segment-wise analysis method: averaged myocardial signal intensities are fitted in each segment. (b) Standard pixel-wise analysis: signal intensities are fitted independently in each pixel. Temporal and/or spatial filtering can be used before the fitting. (c) Proposed method: pixel-wise quantification of unfiltered data. Linearized fitting and Tikhonov regularization are carried out simultaneously. Beforehand, an initial parameter guess is obtained by fitting the SVD-approximated curves in each pixel.

were determined heuristically in the mentioned work.

In this paper, we propose a new approach to stabilize the quantification of perfusion that is based on a spatial Tikhonov regularization and makes use of the fact that neighboring pixels display similar characteristics (see Fig. 1(c)). Fitting and filtering are done simultaneously allowing to continuously balance the outcome of both processes. Another advantage of the Tikhonov regularization is that the strength of regularization can be chosen automatically by means of the L-curve criterion (Hansen & OLeary 1993). Section 2 of this paper introduces the Tikhonov regularization after describing the preprocessing of data and giving a recapitulation of the basis of perfusion quantification.

The performance of our method is evaluated with a numerical phantom showing that our method significantly decreases the root-mean square error of the parameter estimates for appropriate regularization strength. We then applied the method to the data sets of five patients. Section 3 describes the acquisition of patient data and the design of the numerical phantom, while Sec. 4 presents the results of the numerical phantom as well as the patient data. We conclude with a discussion of our method in Sec. 5.

2. Methods

The method we propose for pixel-wise quantification of perfusion is based on a Tikhonov regularization, which makes use of the spatial smoothness of the data: the essential

idea is that during the fitting process, configurations where neighboring pixels display similar parameter values are favored compared to spatially heterogeneous ones. For this fit we used the Fermi method (Jerosch-Herold, Wilke, Stillman & Wilson 1998), the most frequently used method for perfusion quantification. The resulting minimization problem is typically characterized by several local minima and, thus, depends crucially on the choice of the initial guess. An appropriate initial guess was obtained by a single pixel fit of approximated data, where we made use of an approximation with the help of a truncated singular-value decomposition (SVD).

In summary, we suggest the following steps for the analysis of the data

(i) Preprocessing including the choice of time windows of the pre-bolus (for the arterial input function (AIF)) and the main bolus (for the myocardial signal) and the subtraction of a baseline.

(ii) Approximation of the preprocessed data with the first few components of an SVD, i.e., with a truncated SVD.

(iii) Single pixel fit to the SVD-approximated data using the Fermi method.

(iv) Fitting a linearized model at the values obtained in the single-pixel fit in (iii) to the preprocessed data, i.e., not SVD-approximated data, under stabilization with a Tikhonov regularization.

Below these steps are explained in detail.

2.1. Preprocessing

The time windows of the pre-bolus (for the AIF) and the main bolus (for the myocardial signal) were chosen by hand from signal intensities curves averaged over the left ventricular cavity and the myocardium, respectively (see Sec. 3.1 for an explanation of the dual bolus scheme). On average, 47 dynamics were included in the analysis. The dynamics that were acquired late, and were therefore affected by breathing artefacts, were excluded. A horizontal baseline was subtracted in each pixel such that the myocardial signal at the beginning of the main bolus was zero. Note that this can yield negative signal intensities in the presence of noise. However, since we considered an offset as an additional fitting parameter (see Sec. 2.3) this is not a problem. The subtraction of a baseline during the preprocessing only serves as a rough estimate of a baseline and is later improved by the offset fit. The pre-bolus of the AIF was multiplied by ten as the amount of contrast agent in the main bolus was ten times higher than in the prebolus. The AIF was then shifted by a constant time shift Δ_τ, such that the pre-bolus of the AIF and the myocardial signal following the main bolus of contrast coincide. Figure 2(c) shows the time series that is presented as raw data in Fig. 2(b) after having been preprocessed following the above steps. Only the time window of the main bolus of the myocardial signal and the shifted pre-bolus of the AIF is used for the fitting, and therefore, only the signal curves inside this time window are shown.

2.2. SVD approximation

Because of the low SNR, the fit with the Fermi method is often characterized by multiple local minima meaning that the result depends strongly on the initial guess of parameters. To obtain a good initial guess, we carried out a single pixel fit of approximated data as a preprocessing step before carrying out the Tikhonov regularization. We approximated the myocardial signal intensity $c(t, x)$ by its first few principal components obtained with a SVD, i.e., a truncated SVD. To this end, we rewrote $c(t, x)$ as a matrix with elements $C_{ij} \equiv c(t_i, x_j)$, $i = 1, \ldots, m$, $j = 1, \ldots, n$, where t_i is the ith time point when an MR image has been recorded and x_j is the position of the jth pixel. m is the number of time points considered in the analysis, and n the number of pixels in the myocardium, i.e., the region of interest. The SVD reads

$$C = U\Sigma V^T, \tag{1}$$

where U is an $m \times m$ unitary matrix, and V^T is a $n \times n$ unitary matrix. Σ is a $m \times n$ diagonal matrix with the sorted singular values of c on its diagonal. The approximated matrix can be written as

$$\tilde{C} = U\tilde{\Sigma}V^T, \tag{2}$$

where $\tilde{\Sigma}$ is matrix with elements $\tilde{\Sigma}_{ii} = \Sigma_{ii}$, $i = 1, \ldots, k$, and zeros otherwise. Thus, for the approximation we only take the first k largest components into account. Throughout this paper, we chose $k = 4$, since for $k > 4$ the singular values quickly approach zero.

2.3. Deconvolution and Fermi method

Assuming a linear, time invariant system the myocardial signal $c(t, x)$ and the arterial input function $c_a(t)$ are related as

$$c\left(t_i, x_j\right) = \int_0^t c_a\left(t_i - s\right) R\left(s, x_j\right) ds, \tag{3}$$

where $R(t, x_j)$ is the response function of the jth pixel. Myocardial perfusion in the jth pixel can be determined as the maximum of the response function $R(t, x_j)$ (Lee & Johnson 2009). The process of obtaining $R(t, x_j)$ from Eq. (3) is referred to as deconvolution. Unfortunately, a straightforward solution in Fourier space is mathematically unstable. Therefore, various approaches have been suggested to carry out a stable deconvolution. Here, we choose the Fermi method (Jerosch-Herold et al. 1998) that is easy to implement and provides an accurate estimate of perfusion for sufficiently high SNR; as such it is widely used in research (Christian, Rettmann, Aletras, Liao, Taylor, Balaban & Arai 2004, George, Jerosch-Herold, Silva, Kitagawa, Bluemke, Lima & Lardo 2007, Lockie, Ishida, Perera, Chiribiri, De Silva, Kozerke, Marber, Nagel, Rezavi, Redwood & Plein 2011, Biglands, Magee, Sourbron, Plein, Greenwood & Radjenovic 2015, Cookson, Lee, Michler, Chabiniok, Hyde, Nordsletten & Smith 2014, Papanastasiou, Williams, Kershaw, Dweck, Alam, Mirsadraee, Connell, Gray, MacGillivray, Newby & Semple 2015, Schuster, Sinclair,

Zarinabad, Ishida, van den Wijngaard, Paul, van Horssen, Hussain, Perera, Schaeffter et al. 2015, Papanastasiou, Williams, Dweck, Alam, Cooper, Mirsadraee, Newby & Semple 2016). The Fermi method models the response function as a Fermi function

$$R\left(t, x_j\right) \equiv R_F(t; F_j, \tau_j, k_j) = F_j \left[\frac{1}{\exp\left[\left(t - \tau_j\right) k_j\right] + 1}\right] \Theta\left(t - \tau_j\right), \qquad (4)$$

where F_j is proportional to the rate of perfusion in the jth pixel, $\Theta\left(t - \tau_j\right)$ is the Heaviside function, τ_j is the delay between the left ventricular signal and the arrival at the jth pixel of the myocardium and k_j is the decay rate of $R\left(t, x_j\right)$. Since we time-shifted the AIF of the pre-bolus to coincide with the mean myocardial main bolus, τ_j might be negative in some of the pixels. Note that we use a simplified three parametric version of the Fermi function instead of the more commonly used four parametric one, since the low SNR of single pixel curves makes a reasonable fit of four parameters questionable. In fact, the fit with the four parametric version did not yield significantly better fit results than the fit with the three parametric one. Furthermore, the additional parameter τ_0 of the four parametric version, that describes the width of the shoulder of the Fermi function, has no physiological meaning.

Then the following functional is minimized

$$\sum_i \left(c\left(t_i, x_j\right) - \int_0^t c_a\left(t_i - s\right) R_F\left(s; F_j, \tau_j, k_j\right) ds + \delta_j \right)^2 \qquad (5)$$

for each x_j with respect to the parameters of the Fermi function, i.e., F_j, τ_j, and k_j, and the constant offset δ_j. Here this is done with the Levenberg-Marquardt nonlinear least-square algorithm (Wright & Nocedal 1999). The myocardial perfusion in the jth pixel is then given by $F_j/2$.

2.4. Single pixel fit

The curves $\tilde{c}(t, x)$ obtained by the SVD-approximation were fitted pixel-wise with the help of the Fermi function resulting in a first approximation of the parameters in the jth pixel to which we refer as $\theta_j^0 \equiv (F_k^0, k_j^0, \tau_j^0, \delta_j^0)$ in what follows.

2.5. Tikhonov regularization

The Tikhonov regularization improves the results obtained in the single-pixel fit to the SVD-approximated data. It is applied to the preprocessed data – the data after baseline subtraction and choice of pre- and main bolus time windows but without using the SVD-approximation.

Due to the low SNR some of the single pixel fits discussed in the last paragraph are still unstable yielding unphysically high or low parameter estimates because the fitting algorithm gets trapped in local minima. The spatial Tikhonov regularization can remove these outliers due to the additional information of spatial smoothness. Even though with the Tikhonov regularization the fitting algorithm will not necessarily end

at the global minimum, our experience shows that in all observed cases it does end at least in a local minimum much closer to the global one.

For the Tikhonov regularization, we linearized model (3) around the solution obtained in the single-pixel fit to the SVD-approximated data

$$c(t, x_j; \theta_j^0 + \Delta\theta_j) = \widehat{c}_0(t, x_j; \theta_j^0) + J_{\theta_j^0} \Delta\theta_j, \tag{6}$$

where $\widehat{c}_0(t, x; \theta_j^0)$ is the myocardial signal obtained in the single pixel fit, i.e., $\hat{c}_0(t, x_j; \theta_j^0) = \int_0^t c_a(t-s) R\left(s; F_j^0, \tau_j^0, k_j^0\right) ds + \delta_j^0$. $\Delta_j\theta \equiv \theta_j - \theta_j^0$, where $\theta_j = (F_j, k_j, \tau_j, \delta_j)$ is the unknown set of parameters in the jth pixel that we want to estimate. $J_{\theta_j^0}$ is the Jacobian of $c(t, x; \theta_j^0 + \Delta\theta_j)$ with respect to θ_j evaluated at $\Delta\theta_j = 0$.

We then minimize

$$\sum_j ||c(t, x_j) - \widehat{c}_0(t, x_j; \theta_j^0) - J_{\theta_j^0} \Delta\theta_j||^2 + \lambda(\theta^0 + \Delta\theta)^T (K \otimes H)(\theta^0 + \Delta\theta) \tag{7}$$

with respect to $\Delta\theta_j$, where $\theta = (\theta_1, \ldots, \theta_n)^T$, $\theta^0 = (\theta_1^0, \ldots, \theta_n^0)^T$, and $\Delta\theta = (\Delta\theta_1, \ldots, \Delta\theta_n)^T$. $||\cdot||$ denotes the Euclidean 2-norm, and $\otimes$ the Kronecker product. The second term in Eq. (7) corresponds to the Tikhonov regularization: K is the $n \times n$ structure matrix in an intrinsic Gaussian Markov random field prior (Rue & Held 2005) with

$$K_{ij} = \begin{cases} -1, & \text{if } i \neq j, \text{and the } i\text{th and } j\text{th pixel are neighbors,} \\ -\sum_{j, j \neq i} K_{ij}, & \text{if } i = j, \\ 0, & \text{otherwise.} \end{cases} \tag{8}$$

We only consider direct neighbors, i.e., each pixel has eight neighbors (unless it is situated on the boundary of the image), to obtain a high spatial resolution. H is a 4×4 diagonal matrix which balances the strength of the regularization between the four parameters F, k, τ, and δ with H_{11} being the inverse of the median over the squared elements of the vector $K(F_1^0, \ldots, F_n^0)^T$. H_{22}, H_{33}, and H_{44}, are the analogous expressions for k, τ, and δ, respectively. The regularization term is zero if all pixels display the same θ_j values, and increases as the spatial heterogeneity of the parameters rises. Thus, the result is a compromise between the best fit to the data and the spatial smoothness of the estimated parameters.

An appropriate regularization parameter λ can be chosen by means of the L-curve criterion (Hansen & OLeary 1993). The L-curve depicts on a logarithmic scale the regularization term without λ, i.e., $\theta^T(K \otimes H)\theta$, vs. the fit error, i.e., $\sum_j ||c(t, x_j) - \widehat{c}_0(t, x_j; \theta_j^0) - J_{\theta_j^0} \Delta\theta_j||^2$, while changing λ continuously. For small λ the regularization term is usually large and the fitting error is small, while for large λ the regularization term tends to zero but the fitting error normally becomes unacceptably large. Therefore, good choices of λ are the intermediate values, where the regularization and the error terms balance and are both small. An appropriate λ can be determined automatically as the point of largest curvature of the L-curve which we denote as λ_L in what follows.

Note that the spatial regularization presented here is different to the temporal Tikhonov regularization proposed by others when fitting the data (Calamante, Gadian

& Connelly 2003, Pack, DiBella, Rust, Kadrmas, McGann, Butterfield, Christian & Hoffman 2008).

3. Data acquisition

3.1. Patient data

3.1.1. Acquisition Clinical data were obtained from patients of angina symptoms referred to first-pass contrast-enhanced CMR to evaluate the presence of hemodynamically significant coronary artery disease. Three short-axis slices (apical, mid cavity and basal) were acquired on a 3T MR-scanner (Philips Medical, the Netherlands) applying a saturation recovery sequence. More specifically a saturation-recovery gradient-echo was used with 5-fold k-t sensitivity encoding [k-t SENSE], an echo time of TE=0.9 ms, a repetition time of TR=2.6 ms, a flip angle of 20°, a typical spatial resolution of $1.2 \times 1.2 \times 8$ mm^3, and a field of view of 346×346 mm^2. Acquisition of data was ECG triggered to systole, adapted to each patient. The averaged time between dynamics was 0.94 s. The averaged total acquisition time was 106 s. Patients were asked to hold their breath during the main bolus.

As suggested by Ishida et al. (Ishida, Schuster, Morton, Chiribiri, Hussain, Paul, Merkle, Steen, Lossnitzer, Schnackenburg et al. 2011), we used a universal dual bolus-injection scheme with a prebolus of 0.0075 mEq of Gadolinium/kg of body weight and a bolus of 0.075 mEq of Gadolinium/kg of body weight to minimize saturation effects in the AIF. The AIF is determined during the pass of the pre-bolus data and is multiplied by ten (the ratio between the amount of contrast agent in the pre-bolus and in the main bolus), while the myocardial signal is considered during the pass of the main bolus. The advantage of the dual bolus scheme is that the AIF signal, that is much higher than the myocardial signal for the same amount of contrast agent, can be measured without noticeable saturation because only the lower pre-bolus is considered, while the response in the myocardium is still strong enough because it is measured during the main bolus.

Gadolinium chelates (Gadobutrol GadovistVR , Bayer Schering, Germany) were used as a contrast agent. Data were obtained during stress, where stress was induced by a intravenous dose of adenosine of 140 µg/kg body weight/min.

For comparison with the quantitative results, we identified perfusion defects directly from the MR images. To this end, defects were defined visually from all dynamics as a delayed and weakened wash-in of contrast agent.

Figure 2 presents a typical example of data from the mid-cavity slice of one patient. The MR signal at a selected time point is shown in panel (a). Clearly visible is a large defect in segments 8 and 9 (mid-intraventricular septum) (Cerqueira, Weissman, Dilsizian, Jacobs, Kaul, Laskey, Pennell, Rumberger, Ryan & Verani 2002). Panel (b) depicts the time curves of a pixel in the defect (green circles), and a pixel in the healthy myocardium (blue squares), and with red asterisks the arterial input function (AIF). The corresponding pixels are marked by a green circle and blue square in panel (a),

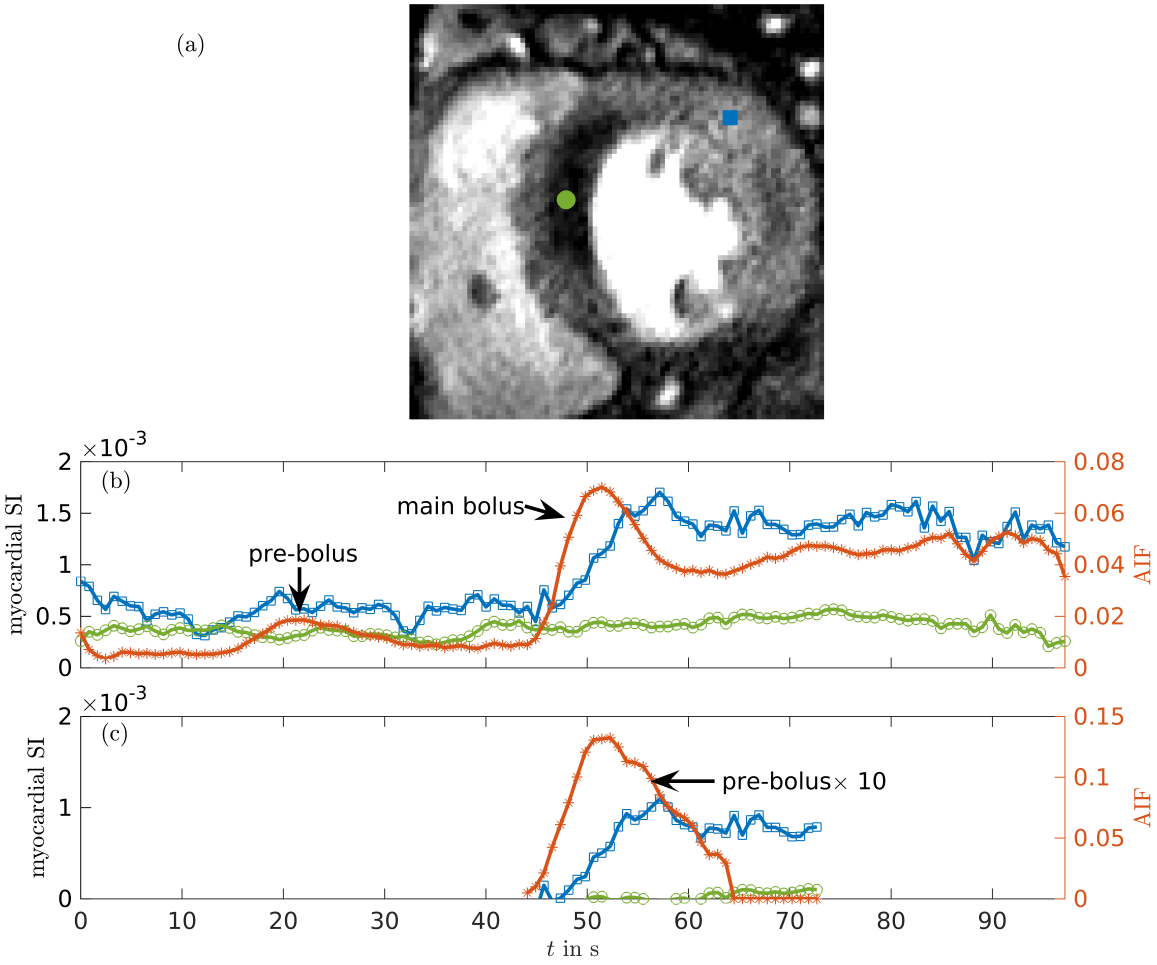

Figure 2. Patient data: (a) Myocardial signal at $t = 58$ s. The blue square and the green circle mark the position of the blue and green time series in panel (c), respectively. (b) Time series of raw data: Red asterisks correspond to arterial input function (AIF) determined in the blood pool. The blue squares show the time series of the healthy myocardium at the position of the blue symbol in (a). The green circles depict the time series in the perfusion defect as marked by the green symbol in (a). (c) As in panel (b) but after the preprocessing steps described in Sec. 2.1.

respectively. The dual bolus scheme is recognizable in the two peaks in the AIF and to a lesser extent in the myocardial signal intensity curves.

3.1.2. Segmentation To acquire the myocardial signal $c(t, x)$ at time t and position x each slice was segmented by hand using OsiriX Imaging software (Pixmeo SARL, Bernex, Switzerland) marking the endocardial and epicardial boundaries to separate the myocardium from the blood pool and the lung. This segmentation step is necessary because the MR signal in the blood pool is much higher than in the myocardium, and, thus, would dominate the SVD-approximation as well as the Tikhonov regularization. Furthermore, the segmentation makes the numerical routine less time consuming. The

AIF $c_a(t)$ was obtained by averaging an ellipsoidal region, selected by hand, in the blood pool of the basal slice (Nooralipour 2013).

3.2. Numerical phantom

We obtain a numerical phantom by choosing appropriately the parameters of the Fermi function in each pixel and then convoluting the Fermi function with the AIF to obtain the myocardial signal. To ensure a realistic spatial distribution of perfusion, we utilized the results obtained in the analysis of one of the patients as the chosen parameters. Figure 3(a) shows the corresponding parameters of the Fermi model, that is explained in Sec. 2.3. The patient we considered (the same for which the clinical data was shown in Fig. 2) has one large perfusion defect that is marked by a red irregular boundary in Fig. 3(b). In addition to this defect, we added artificial perfusion defects of different sizes by setting the F- and τ-values of the Fermi model in the corresponding pixels to the average F- and τ-values in the actual perfusion defect, namely $F = 0.12$ ml/ml/min and $\tau = 2.7$ s. The position of these defects is shown by a yellow squared boundary in Fig. 3(b). From these parameters, we obtained the myocardial signal by convoluting the AIF (using only the scaled pre-bolus) of the patient data set with the Fermi function. We then added spatially homoscedastic noise to the myocardial signal and to the AIF (see Fig. 3(b)), where we chose a ten times higher SNR for the AIF since the AIF is typically averaged over a region in the blood pool making it less noisy. Thus, the myocardial signal in the jth pixel is obtained as

$$c\left(t_i, x_j\right) = \int_0^t c_a\left(t_i - s\right) F_j \left[\frac{1}{\exp\left[\left(s - \tau_j\right)/k_j\right] + 1}\right] \Theta\left(s - \tau_j\right) ds + \xi(t, x_j), \quad (9)$$

where $\xi(t, x_j)$ models the Gaussian white noise in the jth pixel with a SNR defined by $\mathrm{SNR} = \max_{i,j} c\left(t_i, x_j\right)/\tilde{\sigma}$, where $\tilde{\sigma}$ is the standard deviation of ξ. This means that the denoted SNR is defined with respect to the pixel with the largest signal. Thus, the effective SNR in the defect is much smaller than the one in the healthy myocardium. To be more precise, the SNRs of 3, 5, and 15, related to the maximum over all concentration curves, correspond to averaged SNRs of 0.57, 0.95, and 2.86 in the healthy myocardium, and SNRs of 0.10, 0.17, and 0.51 in the underperfused regions, respectively. For the patient data, an averaged SNR of 1.25 was obtained over the whole myocardium.

The AIF (red asterisks) and example time curves in the healthy myocardium (blue squares) and in a perfusion defect (green circles), are shown in see Fig. 3(c).

4. Results

4.1. Numerical phantom

The analysis of the numerical phantom followed the method outlined in Sec. 2. Figure 4(a) shows the L-curve, where the red circle marks the selected λ_L chosen as the point of maximum curvature of the L-curve. We calculated the root mean square

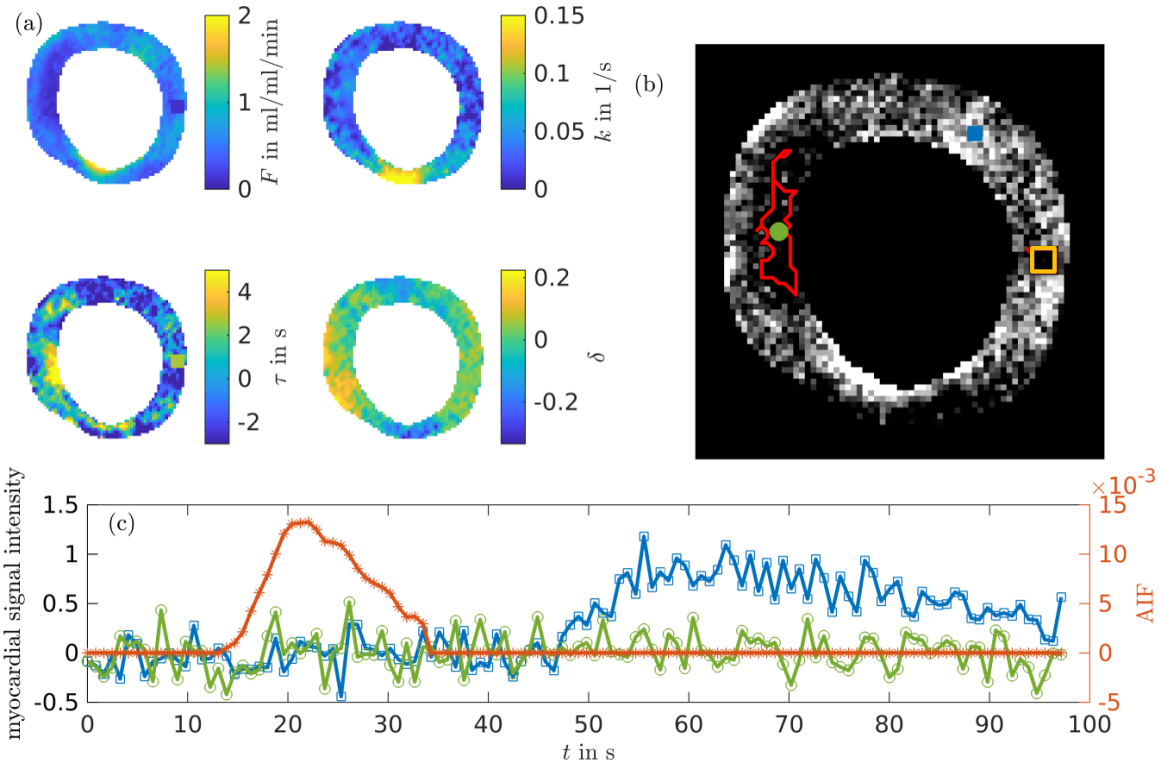

Figure 3. Numerical phantom: (a) Values of the input parameters of the Fermi model F, k, τ, and offset δ, respectively. (b) Myocardial signal at $t = 76$ s. The blue square and the green circle mark the position of the blue, and green timeseries in panel (c), respectively. The red irregular boundary depicts the perfusion defect; the yellow square marks the position of additional artificial perfusion defects. (c) Time series: The blue squares show the time series of the healthy myocardium at the position of the blue symbol in (b). The green circles depict the time series in the defect as marked by the green symbol in (b). The red asterisks correspond to arterial input function (AIF) obtained from patient data. $SNR = 15$ for myocardial signal and $SNR = 150$ for the AIF.

error (RMSE) of F as $\sqrt{\sum_{j,k}(F_j - \widehat{F}_{j_k})^2/n}$, where F_j is the true value of F in the jth pixel, $\widehat{F}_{j_k}$ is the value of F determined by the deconvolution in the jth pixel and in the kth realization, and n is the number of pixels in the myocardium. As anticipated the RMSE has a distinct minimum for an intermediate λ, which is marked as a green cross in Fig. 4(b) and is close to the chosen λ_L determined by the L-curve criterion, confirming the viability of choosing an appropriate λ-value by this criterion. Note that the calculated point of largest curvature, λ_L , does not coincide with the point of largest curvature one would visually select. The reason is that x-axis and y-axis are depicted on different scales making the visual curvature deceptive

In Fig. 5, the results of different fitting methods for SNR=3 ((b)-(d)), SNR=5 ((e)-(g)), and SNR=15 ((h)-(j)) are compared with the true values F ((a)), see also Fig. 3(a) for the true values. As in Fig. 3(b) the large perfusion defect on the left hand side is marked by a red irregular boundary, and the smaller one on the right hand side

by a yellow square. In (b),(e), and (h) the results of the fit to the preprocessed data are presented. A large amount of poorly fitted pixels are visible. In particular, the $\widehat{F}$-values in the large perfusion defect on the left hand side (red irregular boundary) are increased compared to the surrounding area, while the true values are decreased. This effect is most pronounced for SNR=3 but also visible for the larger SNRs. (d), (g), and (j) correspond to the fit to the SVD-approximated data which is already a large improvement, but still some outliers are present for SNR=3 and SNR=5. The Tikhonov regularized fit is shown in (d), (g), and (j) and resembles closely the true values. The large defect (red irregular boundary) is easy to identify and also the smaller defect (yellow squared boundary) is visible in the $\widehat{F}$-values. For SNR=15, no large difference between the regularized fit and the fit to the SVD-approximated data is observed as the latter one is already quite good.

Figure 6 compares the RMSE of the different defects, the healthy myocardium, and the whole myocardium, for different SNRs. Defects 1, 2, and 3, are a 1-pixel, a 3×3-pixels, and a 5×5-pixels defect, respectively, located at the yellow square in Fig. 3(b) for 100 realizations. Defect 4 is the large defect marked by the red irregular boundary in Fig. 3(b). The blue bar depicts the RMSE of a fit to the preprocessed data, while the red bar denotes that of the single pixel fit to the SVD-approximated data, and the yellow bar that of the Tikhonov regularized solution. Obviously, the fit to the preprocessed data is very unstable due to many local minima of the functional (5) causing a large fraction of fits to fail, and the resulting RMSE can be a multiple of the actual perfusion value. Clearly visible, the error is reduced in the single pixel fit to the SVD-approximated data compared to the preprocessed data fit, and is further decreased by the regularization. This behavior is observed in all defects and for all considered SNRs except for defects 1-3 for an SNR of 15. For high SNRs the fit to SVD-approximated data yields already very good results such that a stabilization with the regularization is not necessary anymore. In fact, in defects 1-3, that are only a few pixels in size, the regularization causes the $\hat{F}$-values inside the defect to increase to values higher than the actual values in the defect to match the values outside the defect in the healthy myocardium. By comparing the magnitude of the RSME of our method to that of the other methods, a critical defect size can be estimated below which this overregularization effect sets in. Furthermore, a comparison of the RMSEs of the different methods allows for determining the amplitude of this effect.

We also compared our technique to an alternative method where we smoothed the image before doing a single-pixel-fit. The smoothing was done by placing a 3x3 patch around each pixel and averaging over all the pixels in this patch which significantly reduces the noise. However, it showed that the resulting RMSE is significantly higher than in our method though lower than in the fit to the raw data. To keep the figure concise, we did not include these results in Fig. 6.

The spatial distribution of the RMSE of the different methods is compared in Fig. 7, where we calculated the RMSE in the jth pixel as $\sqrt{\sum_k (F_j - \widehat{F}_{j_k})^2/n}$. Subfigures 7(a)-(c) show the RMSE of F, while (d)-(f) depict the RMSE of τ. The largest RMSE of F

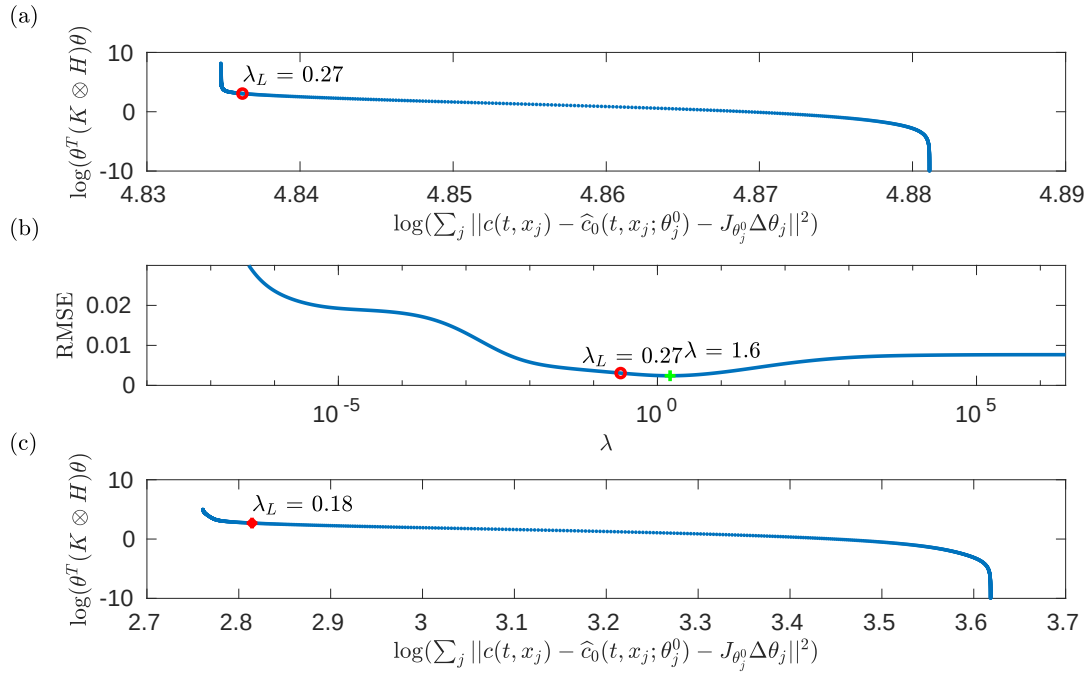

Figure 4. L-curves. (a) L-curve for numerical phantom. The red circle marks λ_L, the λ chosen by the L-curve criterion. (b) Root mean square error (RMSE) in F vs. λ for the numerical phantom. The red circle denotes λ_L, and the green cross marks the minimum of the RMSE-curve. (c) L-curve for patient data. The red circle marks λ_L. SNR= 5 in (a) and (b). Other parameters as in Fig. 3.

and τ can be observed when fitting the preprocessed data (see Fig. 7(a) and Fig. 7(d), respectively). Particular high RMSEs are present in the perfusion defects marked by the yellow square and red irregular boundary in Fig. 3(b). The RMSEs are reduced in the fit to the SVD-approximated data (see Fig. 7(b) and Fig. 7(e), respectively). However, the perfusion defects are still visible in an increased RMSE. The results of the Tikhonov regularized fit are shown in Fig. 7(c) and Fig. 7(f), respectively: the overall RMSE as well as the RMSE in the defect is further decreased. The RMSE of F is not noticeably higher in the defects compared to the healthy myocardium. The RMSE of τ in the defect is still higher than outside of the defect but significantly smaller than in the other two methods.

4.2. Patient data

As in the numerical phantom, the appropriate regularization parameter λ_L for the patient data was determined by the L-curve criterion. The L-curves for the patient data displayed what was expected as the typical form of an L-curve confirming that the regularization has the desired effect. As an example, the L-curve of one of the patients is shown in Fig. 4(c) with the point of maximal curvature marked by a red circle.

Figure 8 presents the parameter estimates for the patient data: (a) shows the

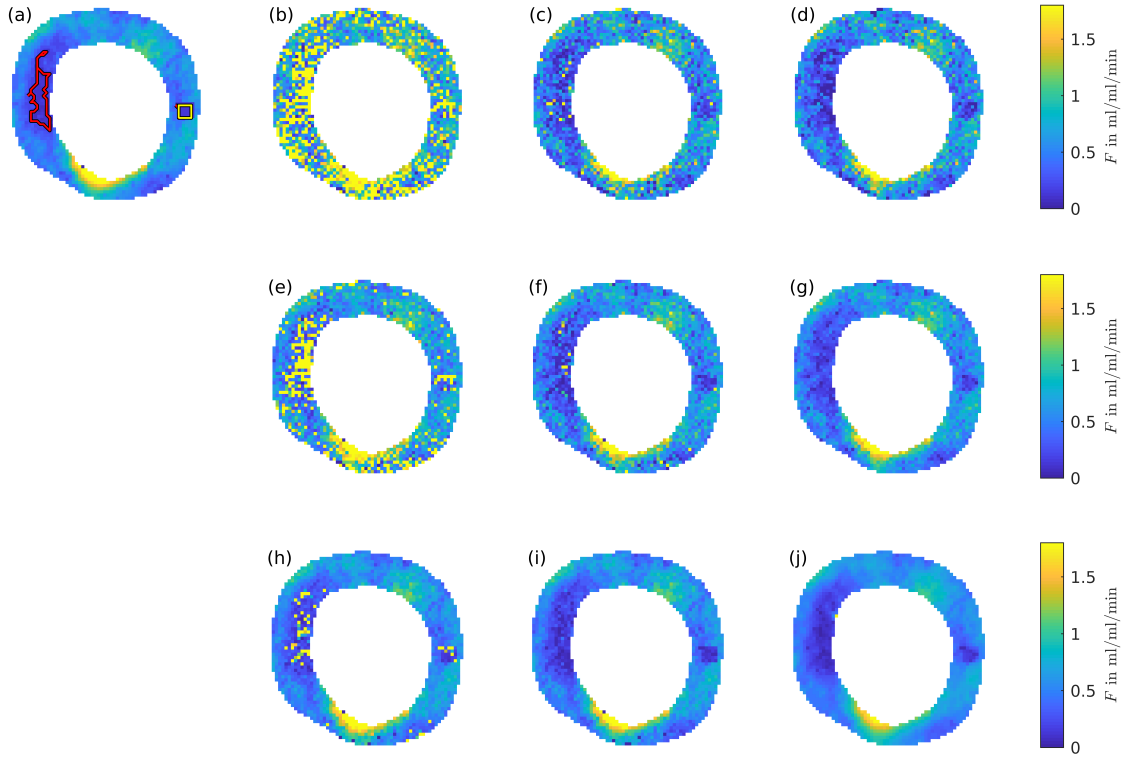

Figure 5. Comparison of different fitting methods for SNR=3 ((b)-(d)), SNR=5 ((e)-(g)), and SNR=15 ((h)-(j)): (a) True value of F, used as input value to the numerical phantom. The red irregular boundary and the yellow square mark the position of perfusion defects. (b),(e), and (h): $\widehat{F}$ as the result of a fit to preprocessed data. (c),(f), and (i): $\widehat{F}$ as the result of a fit to SVD approximated data. (d), (g), and (j): $\widehat{F}$ as the result of a Tikhonov regularized fit as discussed in Sec. 2. The corresponding MR-signal for SNR=15 is shown in Fig. 3(b). $\Delta_\tau = 36.2$ s.

myocardial signal intensities of the apical slice; (b)-(e) show the corresponding $\widehat{F}$-, $\widehat{\tau}$-, $\widehat{k}$-, and offset-values calculated with the here suggested Tikhonov regularization, respectively. As anticipated the $\widehat{F}$-values correlate with the corresponding myocardial signal. A high MR signal means that the region is well perfused, while a low signal indicates a hypoperfused area, an effect that is well reflected in the $\widehat{F}$-values. In contrast, the delay $\widehat{\tau}$ is enhanced in poorly defused regions as can be observed in Fig. 8(d). This behavior can be seen particularly well in the large perfusion defect (marked by a red arrow) on the left, i.e., in standard segment 14 (Cerqueira et al. 2002). Even though a comparison with a ground truth is not possible in case of the patient data, the results are consistent with the myocardial signal and with each other, supporting the soundness of our method.

In Fig. 9(a)-(c) and (d)-(f), the $\widehat{F}$-values and the $\widehat{\tau}$-values resulting from different fitting approaches are compared. Namely, the results of the fit to the preprocessed data are presented in (a) and (d); the outcome of the fit to the SVD-approximated data are shown in (b) and (e); and the results of the Tikhonov regularized fit are depicted in (c)

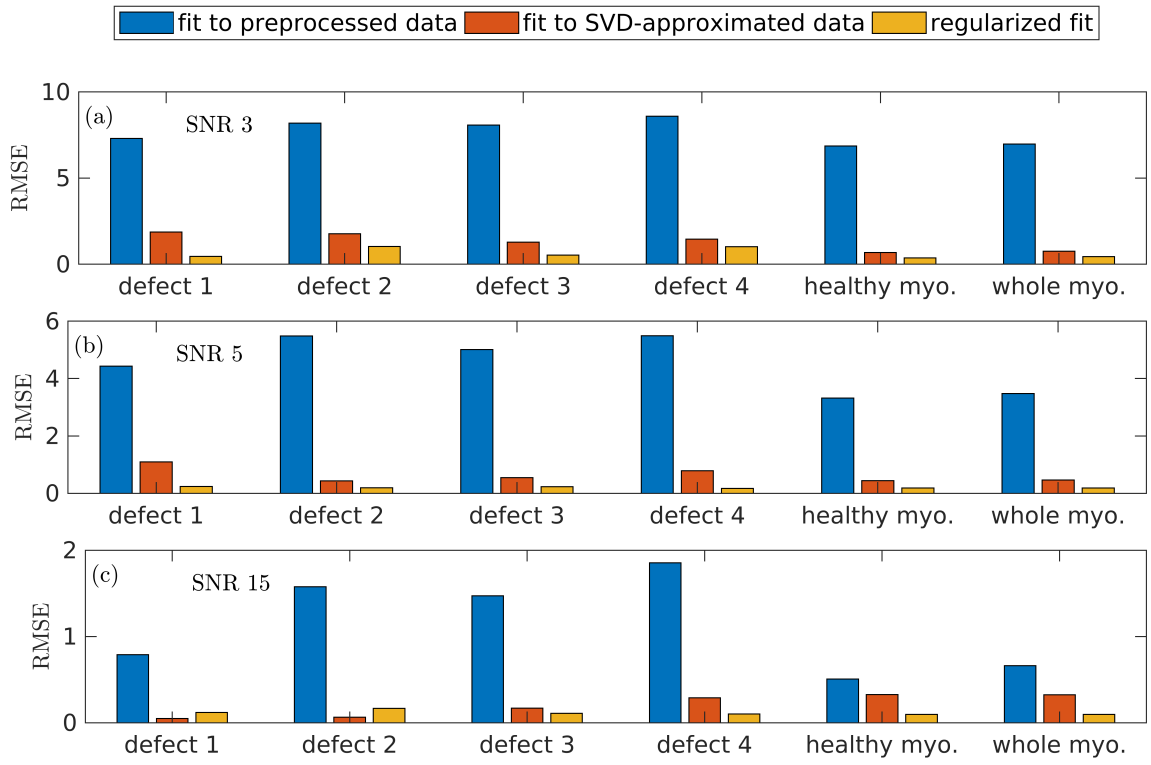

Figure 6. Root mean square error of F obtained from 100 realizations of the numerical phantom in defects 1 to 4, the healthy myocardium, and the whole myocardium, from left to right, and for an SNR of 3, 5, and 15 in (a)-(c), respectively. Blue bar: single pixel fit to the preprocessed data. Red bar: single pixel fit to the SVD-approximated data as described in Sec. 2.4. Yellow bar: Tikhonov regularized results as described in Sec. 2.5. Other parameters as in Fig. 3. Defects 1, 2, and 3, are a 1-pixel, a 3×3-pixel, and a 5×5-pixel defect, respectively, located at the yellow square in Fig. 3(b). Defect 4 is the defect marked by the red irregular boundary in Fig. 3(b).

and (f). The advantage of the Tikhonov regularization is clearly visible. Even though most pixels are also fitted in a sensible way with the two other fitting approaches, there is a non-negligible amount of pixels where those fits fail; this is visible, for example, in the unphysical high $\widehat{F}$-values in some of the pixels inside the perfusion defect seen in (a), and to a lesser extent in (b). A similiar behavior cannot be seen in the myocardial signal shown in Fig. 2(a) and thus cannot be explained by the data. Furthermore, the preprocessed data fit yields decreased $\widehat{\tau}$-values in the perfusion defect, where we would, for physiological reasons, have anticipated elevated values as they were correctly obtained in the fit to the SVD-data (see panel (e)) and in the regularized fit (see panel (f)). The Tikhonov regularization proves to be a much more robust approach where no obvious failure in the fitting is observed. In this way, the regularization gives rise to a clearer picture of the hemodynamical structure present in the data.

To give some more examples of the results obtained with the Tikhonov regularization Fig. 10 shows the outcome for two other patients and the basal slice of the patient shown in Figs. 8 and 9; for the sake of conciseness, we only show one slice

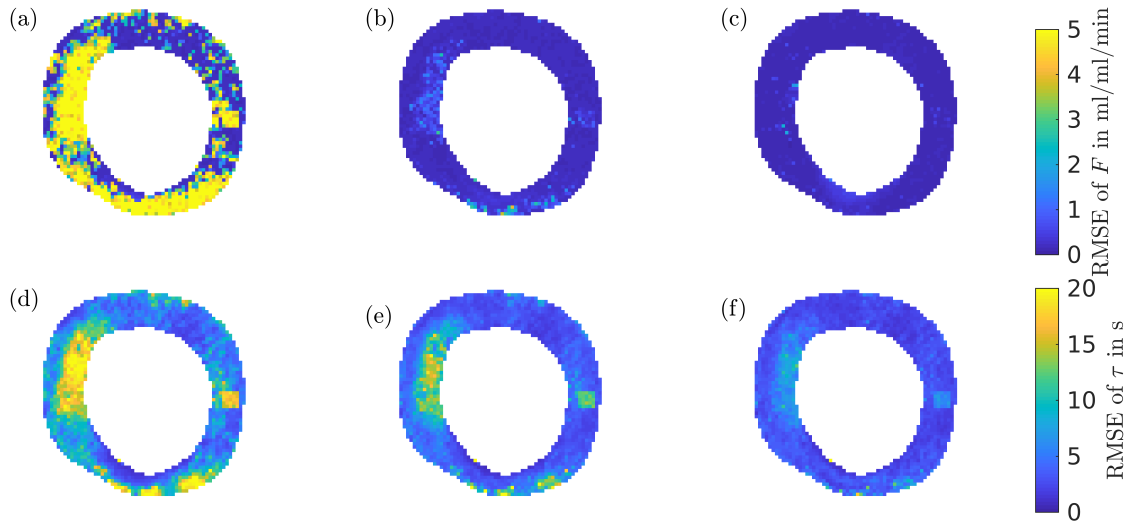

Figure 7. Comparison of different fitting methods in the numerical phantom for SNR 5 and 100 realizations: (a) Pixel-wise RMSE of F as the result of a fit to preprocessed data. (b) Pixel-wise RMSE of F as the result of a fit to SVD approximated data. (c) Pixel-wise RMSE of F as the result of a Tikhonov regularized fit as discussed in Sec. 2. (d) Pixel-wise RMSE of τ as the result of a fit to preprocessed data. (e) Pixel-wise RMSE of τ as the result of a fit to SVD approximated data. (f) Pixel-wise RMSE of τ as the result of a Tikhonov regularized fit as discussed in Sec. 2. Other parameters as in Fig. 3. The corresponding MR-signal is shown in Fig. 3(b).

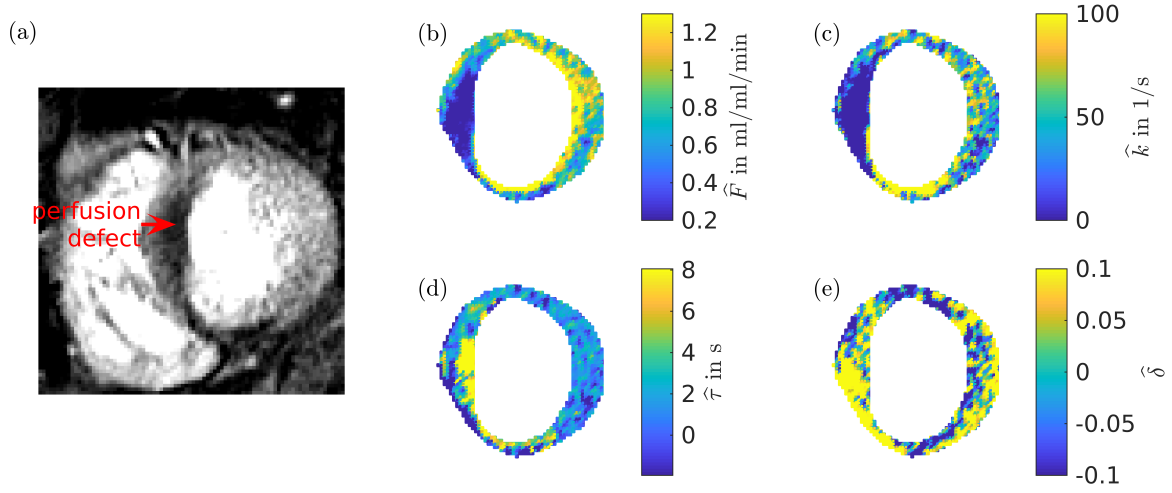

Figure 8. Patient data: (a) Myocardial signal of apical slice at a selected time point. (b) Myocardial perfusion. (c) $\widehat{k}$-values. (d) Delay $\widehat{\tau}$ between blood pool and myocardium. $\Delta_\tau = 26.9$ s. (e) Offset-values.

for each patient and only the $\widehat{F}$-and $\widehat{\tau}$-values. As anticipated $\widehat{F}$ correlates well with the myocardial signal, while $\widehat{\tau}$ anticorrelates with the myocardial signal and $\widehat{F}$.

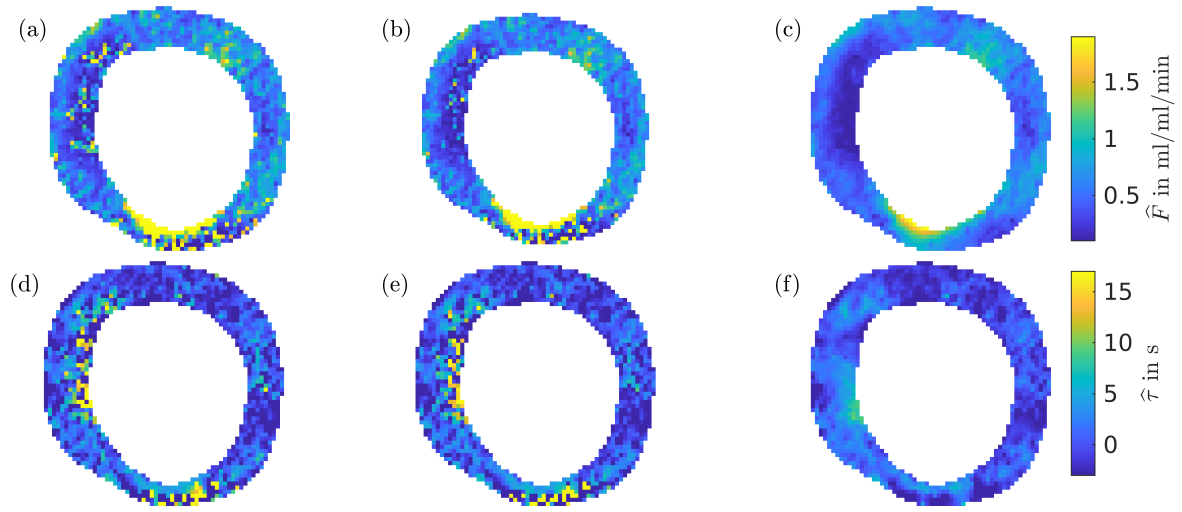

Figure 9. Comparison of different fitting methods: (a) $\widehat{F}$ as the result of a fit to preprocessed data. (b) $\widehat{F}$ as the result of a fit to SVD approximated data. (c) $\widehat{F}$ as the result of a Tikhonov regularized fit as discussed in Sec. 2. (d) $\widehat{\tau}$ as the result of a fit to preprocessed data. (e) $\widehat{\tau}$ as the result of a fit to SVD approximated data. (f) $\widehat{\tau}$ as the result of a Tikhonov regularized fit as discussed in Sec. 2. The corresponding MR-signal is shown in Fig. 2(a). $\Delta_\tau = 36.2$ s.

5. Discussion

We demonstrated pixel-wise quantification of myocardial perfusion by means of a spatial Tikhonov regularization in both simulated and patient data. The challenge of pixel-wise quantification is the typically low SNR. Because of this, most work on pixel-wise quantification of perfusion relies on filtering spatially and/or temporally prior to the deconvolution step (Hsu et al. 2012, Zarinabad et al. 2012, Kellman et al. 2017). In contrast to prefiltering in time and space, the Tikhonov regularization suggested here performs fitting and regularization in one step and, therefore, balances the effects of these two procedures. Whilst errors that are introduced during the filtering that takes place before the fitting will necessarily affect the results, this is not necessarily the case for our method. Instead, the result of the Tikhonov regularization is a balance between the best fit to the (noisy) time curves and the spatial smoothness of the resulting parameters. Compared to methods which forgo any filtering or regularization, the Tikhonov regularization takes into account the spatial smoothness of the parameter as additional information, and this can reduce the errors in the parameter estimation as we were able to show for the numerical phantom.

The method we suggested here is automatic in the sense that the overall strength of the regularization is determined by the L-curve criterion. In the numerical phantom, we showed that the root mean square error in the perfusion values becomes minimal around the value determined by the L-curve criterion, confirming the validity of this criterion.

At the same time, the minimum in the RMSE-vs.-λ-curve demonstrates that the

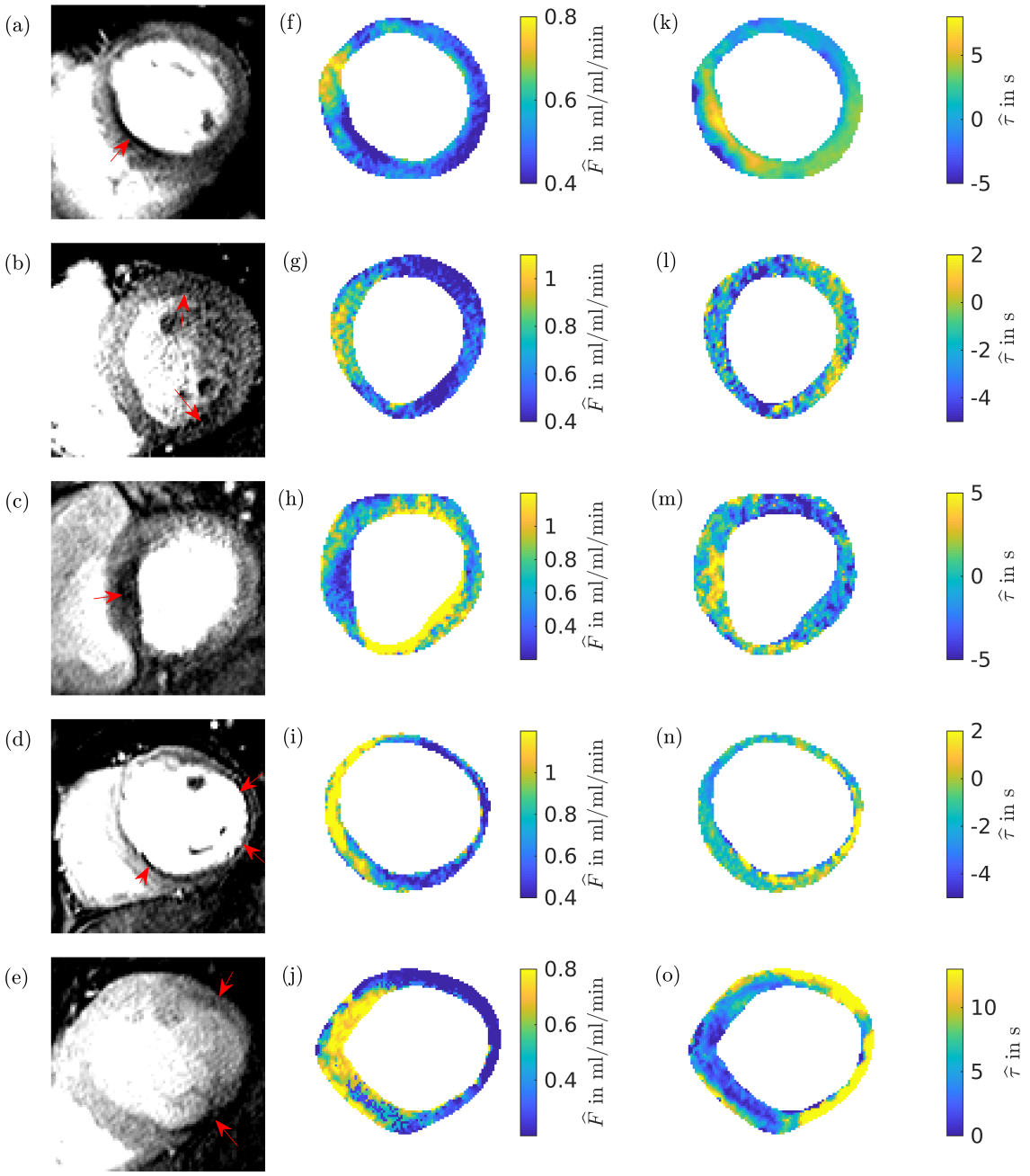

Figure 10. Patient data: (a)-(e) myocardial signal of the basal slice at selected time point of five different patients. Perfusion defects are indicated by red arrows. (f)-(j) Corresponding $\widehat{F}$-values. (k)-(o) Corresponding $\widehat{\tau}$-values. $\Delta_\tau = 27.6$ s, $\Delta_\tau = 32.4$ s, $\Delta_\tau = 30.2$ s, $\Delta_\tau = 34.1$ s, and, $\Delta_\tau = 29.4$ s for the patient presented in (a)-(e), respectiverly.

regularization, in fact, decreases the error of the parameter estimate compared to a non or too weakly regularized fit. This is further confirmed when considering the RMSE in the different defects introduced in the numerical phantom, the healthy myocardium, and the overall myocardium for different SNRs. It shows that the RMSE is reduced in the fit to the SVD-approximated data compared to the preprocessed data. Using the Tikhonov regularization further decreases the RMSE. A different behavior can only be observed for a very good SNR of 15 and very small defect sizes. Here, the RMSE of the regularized results is slightly larger than the one of the results obtained in the fit to the SVD-approximated data, though it is still considerably smaller than the RMSE of the preprocessed data fit. This behavior results from the fact that in the small defects the influence of the healthy environment is too large making the $\widehat{F}$-values in the defect increase. If the SNR is high this effect is larger than the counteracting effect of the stabilization. However, a SNR of 15 is much higher than the SNR in patient data which is typically between 5 and 10. Furthermore, in patient data effects like the dual bolus scheme, the second pass of the contrast agent, respiratory effects, and model errors make stable fitting much harder and, thus, have a similar effect as a reduced SNR.

The quantification of perfusion is very sensitive to the delay (Jerosch-Herold, Hu, Murthy & Seethamraju 2004). In segment-wise deconvolution the delay is often determined by the user from time curves averaged over one segment. In pixel-wise segmentation determining the delay from the segment-wised averaged time curves is too inaccurate, while selecting the delay from the time curves of each pixel is too cumbersome and time intensive. Zarinabad et al. suggested to determine the delay in an outer minimization loop (Zarinabad, Hautvast, Sammut, Arujuna, Breeuwer, Nagel & Chiribiri 2014). Here, this is not necessary since the combination of the single pixel fit to the SVD-approximated data and the Tikhonov regularization ensures that the fit is stable enough to fit the delay τ simultaneously with the other parameters. The results in patient data show that the delay is increased in the perfusion defects, and, thus, might also be an indicator of ischemic regions as has been suggested in (Jerosch-Herold, Hu, Murthy & Seethamraju 2004, Zarinabad et al. 2014).

The deconvolution step, we considered here, is only one step in the analysis of perfusion that does not affect the other steps nor is directly affected by those. Thus, spatial Tikhonov regularization can be easily integrated into other quantification schemes. In particular, automatic segmentation, motion correction or correction for coil sensitivities inhomogeneities could be applied in the analysis beforehand. Another option would be the use of schemes other than the two-bolus scheme to handle the nonlinearity of the signal. For example, a conversion from signal to concentration could be applied subsequently to the acquisition, or the dual sequence approach could be used (Kellman et al. 2017).

The structure matrix K we based the Tikhonov regularization on is also used as a prior of an intrinsic Gaussian Markov Random Field (GMRF) with the same assumption on the spatial smoothness of parameters (Rue & Held 2005). The solution we obtained with the Tikhonov regularization corresponds to the maximum a posteriori estimate one

would obtain treating the problem in a Bayesian formalism with a GMRF prior under appropriate distributional assumptions. Thus, a Bayesian generalization of our method is straightforward. The result of a Bayesian formalism is a probability distribution for each estimated parameter instead of a single value. The uncertainty of the parameter estimation follows naturally from the width of these distributions which is a crucial advantage compared to a non-Bayesian approach. Furthermore, the Bayesian formalism allows to include prior knowledge on the parameters in form of the priors.

Another interesting extension of our work could be modifying the regularization term utilizing the Huber function (Frouin, De Cesare, Bouchareb, Todd-Pokropek & Herment 1999). The Huber function is quadratic for small arguments but linear for larger arguments. This means that for small differences in neighboring pixels, a regularization based on the Huber function would be identical to the here suggested Tikhonov regularization but for larger differences the effect would be weaker compared to the Tikhonov regularization. This could help to reduce the effect of smoothing over physiological borders, for example, between defects and healthy myocardium or between myocardium and blood pool in case that the segmentation misclassified some of the blood pool pixels. However, the use of the Huber function would require choosing a threshold above which the function is linear, and finding an appropriate automatic choice of this threshold would introduce a further challenge.

We conclude that our method is a feasible approach to perform pixel-wise quantification of myocardial perfusion in the presence of low SNR. In future work, we would like to clinically validate our method and treat it within the Bayesian formalism.

Acknowledgment

This work was supported by the EMPIR project 15HLT05 PerfusImaging. The EMPIR initiative is co-funded by the European Union's Horizon 2020 research and innovation programme and the EMPIR Participating States.

Attili, A. K., Schuster, A., Nagel, E., Reiber, J. H. C. & van der Geest, R. J. (2010). Quantification in cardiac mri: advances in image acquisition and processing, *The International Journal of Cardiovascular Imaging* **26**(1): 27–40.
URL: *https://doi.org/10.1007/s10554-009-9571-x*

Biglands, J. D., Magee, D. R., Sourbron, S. P., Plein, S., Greenwood, J. P. & Radjenovic, A. (2015). Comparison of the diagnostic performance of four quantitative myocardial perfusion estimation methods used in cardiac mr imaging: Ce-marc substudy, *Radiology* **275**(2): 393–402. PMID: 25521666.
URL: *http://dx.doi.org/10.1148/radiol.14140433*

Calamante, F., Gadian, D. G. & Connelly, A. (2003). Quantification of bolus-tracking mri: Improved characterization of the tissue residue function using tikhonov regularization, *Magnetic resonance in medicine* **50**(6): 1237–1247.

Cerqueira, M. D., Weissman, N. J., Dilsizian, V., Jacobs, A. K., Kaul, S., Laskey, W. K., Pennell, D. J., Rumberger, J. A., Ryan, T. & Verani, M. S. (2002). Standardized myocardial segmentation and nomenclature for tomographic imaging of the heart, *Circulation* **105**(4): 539–542.
URL: *http://circ.ahajournals.org/content/105/4/539*

Chiribiri, A., Schuster, A., Ishida, M., Hautvast, G., Zarinabad, N., Morton, G., Otton, J., Plein, S.,

Breeuwer, M., Batchelor, P. et al. (2012). Perfusion phantom: An efficient and reproducible method to simulate myocardial first-pass perfusion measurements with cardiovascular magnetic resonance, *Magnetic resonance in medicine* **69**(3): 698–707.

Christian, T. F., Rettmann, D. W., Aletras, A. H., Liao, S. L., Taylor, J. L., Balaban, R. S. & Arai, A. E. (2004). Absolute myocardial perfusion in canines measured by using dual-bolus first-pass mr imaging 1, *Radiology* **232**(3): 677–684.

Cookson, A., Lee, J., Michler, C., Chabiniok, R., Hyde, E., Nordsletten, D. & Smith, N. (2014). A spatially-distributed computational model to quantify behaviour of contrast agents in mr perfusion imaging, *Medical Image Analysis* **18**(7): 1200 – 1216.
URL: *//www.sciencedirect.com/science/article/pii/S1361841514001091*

Dabir, D., Child, N., Kalra, A., Rogers, T., Gebker, R., Jabbour, A., Plein, S., Yu, C.-Y., Otton, J., Kidambi, A. et al. (2014). Reference values for healthy human myocardium using a t1 mapping methodology: results from the international t1 multicenter cardiovascular magnetic resonance study, *Journal of Cardiovascular Magnetic Resonance* **16**(1): 69.

Frouin, F., De Cesare, A., Bouchareb, Y., Todd-Pokropek, A. & Herment, A. (1999). Spatial regularization applied to factor analysis of medical image sequences (famis), *Physics in Medicine & Biology* **44**(9): 2289.

George, R. T., Jerosch-Herold, M., Silva, C., Kitagawa, K., Bluemke, D. A., Lima, J. A. & Lardo, A. C. (2007). Quantification of myocardial perfusion using dynamic 64-detector computed tomography, *Investigative radiology* **42**(12): 815–822.

Greenwood, J. P., Maredia, N., Younger, J. F., Brown, J. M., Nixon, J., Everett, C. C., Bijsterveld, P., Ridgway, J. P., Radjenovic, A., Dickinson, C. J. et al. (2012). Cardiovascular magnetic resonance and single-photon emission computed tomography for diagnosis of coronary heart disease (ce-marc): a prospective trial, *The Lancet* **379**(9814): 453–460.

Gupta, V., Kirişli, H. A., Hendriks, E. A., van der Geest, R. J., van de Giessen, M., Niessen, W., Reiber, J. H. & Lelieveldt, B. P. (2012). Cardiac mr perfusion image processing techniques: a survey, *Medical image analysis* **16**(4): 767–785.

Hansen, P. C. & OLeary, D. P. (1993). The use of the l-curve in the regularization of discrete ill-posed problems, *SIAM Journal on Scientific Computing* **14**(6): 1487–1503.

Hsu, L.-Y., Groves, D. W., Aletras, A. H., Kellman, P. & Arai, A. E. (2012). A quantitative pixel-wise measurement of myocardial blood flow by contrast-enhanced first-pass cmr perfusion imaging: microsphere validation in dogs and feasibility study in humans, *JACC: Cardiovascular Imaging* **5**(2): 154–166.

Hsu, L.-Y., Jacobs, M., Benovoy, M., Ta, A. D., Conn, H. M., Winkler, S., Greve, A. M., Chen, M. Y., Shanbhag, S. M., Bandettini, W. P. et al. (2018). Diagnostic performance of fully automated pixel-wise quantitative myocardial perfusion imaging by cardiovascular magnetic resonance, *JACC: Cardiovascular Imaging* .

Ishida, M., Schuster, A., Morton, G., Chiribiri, A., Hussain, S., Paul, M., Merkle, N., Steen, H., Lossnitzer, D., Schnackenburg, B. et al. (2011). Development of a universal dual-bolus injection scheme for the quantitative assessment of myocardial perfusion cardiovascular magnetic resonance, *Journal of Cardiovascular Magnetic Resonance* **13**(1): 28.

Jerosch-Herold, M. (2010). Quantification of myocardial perfusion by cardiovascular magnetic resonance, *Journal of Cardiovascular Magnetic Resonance* **12**(1): 1.

Jerosch-Herold, M., Hu, X., Murthy, N. S. & Seethamraju, R. T. (2004). Time delay for arrival of mr contrast agent in collateral-dependent myocardium, *IEEE transactions on medical imaging* **23**(7): 881–890.

Jerosch-Herold, M., Seethamraju, R. T., Swingen, C. M., Wilke, N. M. & Stillman, A. E. (2004). Analysis of myocardial perfusion mri, *Journal of Magnetic Resonance Imaging* **19**(6): 758–770.
URL: *http://dx.doi.org/10.1002/jmri.20065*

Jerosch-Herold, M., Wilke, N., Stillman, A. E. & Wilson, R. F. (1998). Magnetic resonance quantification of the myocardial perfusion reserve with a fermi function model for constrained

deconvolution, *Medical physics* **25**(1): 73–84.

Kellman, P., Hansen, M. S., Nielles-Vallespin, S., Nickander, J., Themudo, R., Ugander, M. & Xue, H. (2017). Myocardial perfusion cardiovascular magnetic resonance: optimized dual sequence and reconstruction for quantification, *Journal of Cardiovascular Magnetic Resonance* **19**(1): 43.
URL: *https://doi.org/10.1186/s12968-017-0355-5*

Lee, D. C. & Johnson, N. P. (2009). Quantification of absolute myocardial blood flow by magnetic resonance perfusion imaging, *JACC: Cardiovascular Imaging* **2**(6): 761–770.

Lee, D. C., Simonetti, O. P., Harris, K. R., Holly, T. A., Judd, R. M., Wu, E. & Klocke, F. J. (2004). Magnetic resonance versus radionuclide pharmacological stress perfusion imaging for flow-limiting stenoses of varying severity, *Circulation* **110**(1): 58–65.

Lockie, T., Ishida, M., Perera, D., Chiribiri, A., De Silva, K., Kozerke, S., Marber, M., Nagel, E., Rezavi, R., Redwood, S. & Plein, S. (2011). High-resolution magnetic resonance myocardial perfusion imaging at 3.0-tesla to detect hemodynamically significant coronary stenoses as determined by fractional flow reserve, *Journal of the American College of Cardiology* **57**(1): 70–75.
URL: *http://www.onlinejacc.org/content/57/1/70*

Miller, C. A., Naish, J. H., Ainslie, M. P., Tonge, C., Tout, D., Arumugam, P., Banerji, A., Egdell, R. M., Clark, D., Weale, P., Steadman, C. D., McCann, G. P., Ray, S. G., Parker, G. J. & Schmitt, M. (2014). Voxel-wise quantification of myocardial blood flow with cardiovascular magnetic resonance: effect of variations in methodology and validation with positron emission tomography, *Journal of Cardiovascular Magnetic Resonance* **16**(1): 11.
URL: *http://dx.doi.org/10.1186/1532-429X-16-11*

Nooralipour, N. Z. (2013). *Advanced Quantification of Myocardial Perfusion*, PhD thesis.

Pack, N. A., DiBella, E. V., Rust, T. C., Kadrmas, D. J., McGann, C. J., Butterfield, R., Christian, P. E. & Hoffman, J. M. (2008). Estimating myocardial perfusion from dynamic contrast-enhanced cmr with a model-independent deconvolution method, *Journal of Cardiovascular Magnetic Resonance* **10**(1): 1.

Papanastasiou, G., Williams, M. C., Dweck, M. R., Alam, S., Cooper, A., Mirsadraee, S., Newby, D. E. & Semple, S. I. (2016). Quantitative assessment of myocardial blood flow in coronary artery disease by cardiovascular magnetic resonance: comparison of fermi and distributed parameter modeling against invasive methods, *Journal of Cardiovascular Magnetic Resonance* **18**(1): 57.
URL: *http://dx.doi.org/10.1186/s12968-016-0270-1*

Papanastasiou, G., Williams, M. C., Kershaw, L. E., Dweck, M. R., Alam, S., Mirsadraee, S., Connell, M., Gray, C., MacGillivray, T., Newby, D. E. & Semple, S. I. (2015). Measurement of myocardial blood flow by cardiovascular magnetic resonance perfusion: comparison of distributed parameter and fermi models with single and dual bolus, *Journal of Cardiovascular Magnetic Resonance* **17**(1): 17.
URL: *http://dx.doi.org/10.1186/s12968-015-0125-1*

Plein, S., Schwitter, J., Suerder, D., Greenwood, J. P., Boesiger, P. & Kozerke, S. (2008). K-space and time sensitivity encoding–accelerated myocardial perfusion mr imaging at 3.0 t: comparison with 1.5 t, *Radiology* **249**(2): 493–500.

Rue, H. & Held, L. (2005). *Gaussian Markov random fields: theory and applications*, CRC press.

Sammut, E., Zarinabad, N., Wesolowski, R., Morton, G., Chen, Z., Sohal, M., Carr-White, G., Razavi, R. & Chiribiri, A. (2015). Feasibility of high-resolution quantitative perfusion analysis in patients with heart failure, *Journal of Cardiovascular Magnetic Resonance* **17**(1): 13.

Schuster, A., Sinclair, M., Zarinabad, N., Ishida, M., van den Wijngaard, J. P., Paul, M., van Horssen, P., Hussain, S. T., Perera, D., Schaeffter, T. et al. (2015). A quantitative high resolution voxel-wise assessment of myocardial blood flow from contrast-enhanced first-pass magnetic resonance perfusion imaging: microsphere validation in a magnetic resonance compatible free beating explanted pig heart model, *European Heart Journal-Cardiovascular Imaging* **16**(10): 1082–1092.

Schwitter, J., Wacker, C. M., van Rossum, A. C., Lombardi, M., Al-Saadi, N., Ahlstrom, H., Dill, T., Larsson, H. B., Flamm, S. D., Marquardt, M. et al. (2008). Mr-impact: comparison of

perfusion-cardiac magnetic resonance with single-photon emission computed tomography for the detection of coronary artery disease in a multicentre, multivendor, randomized trial, *European heart journal* **29**(4): 480–489.

Sourbron, S. & Buckley, D. L. (2012). Tracer kinetic modelling in mri: estimating perfusion and capillary permeability, *Physics in medicine and biology* **57**(2): R1.

Villa, A. D., Sammut, E., Shome, J. S., Razavi, R., Plein, S. & Chiribiri, A. (2016). Combined high-resolution assessment of quantitative perfusion and late enhancement. towards accurate estimation of the ischaemic burden in patients with coronary artery disease, *Journal of Cardiovascular Magnetic Resonance* **18**(422).

Wright, S. & Nocedal, J. (1999). Numerical optimization, *Springer Science* **35**(67-68): 7.

Zarinabad, N., Chiribiri, A., Hautvast, G. L., Ishida, M., Schuster, A., Cvetkovic, Z., Batchelor, P. G. & Nagel, E. (2012). Voxel-wise quantification of myocardial perfusion by cardiac magnetic resonance. feasibility and methods comparison, *Magn. Reson. Med.* **68**(6): 1994–2004.

Zarinabad, N., Hautvast, G. L., Sammut, E., Arujuna, A., Breeuwer, M., Nagel, E. & Chiribiri, A. (2014). Effects of tracer arrival time on the accuracy of high-resolution (voxel-wise) myocardial perfusion maps from contrast-enhanced first-pass perfusion magnetic resonance, *IEEE Transactions on Biomedical Engineering* **61**(9): 2499–2506.